



OBSERVATION OF A QUASIPERIODIC PULSATION IN HARD X-RAY, RADIO, AND EXTREME-ULTRAVIOLET WAVELENGTHS

PANKAJ KUMAR¹, VALERY M. NAKARIAKOV^{2,3,4}, AND KYUNG-SUK CHO^{1,5}

¹ Korea Astronomy and Space Science Institute (KASI), Daejeon, 305-348, Korea; pankaj@kasi.re.kr
² Centre for Fusion, Space and Astrophysics, Department of Physics, University of Warwick, CV4 7AL, UK
³ School of Space Research, Kyung Hee University, Yongin, 446-701, Gyeonggi, Korea
⁴ Central Astronomical Observatory at Pulkovo of RAS, 196140 St Petersburg, Russia
⁵ University of Science and Technology, Daejeon 305-348, Korea

Received 2015 November 6; accepted 2016 March 4; published 2016 April 26

ABSTRACT

We present a multiwavelength analysis of a quasiperiodic pulsation (QPP) observed in the hard X-ray (HXR), radio, and extreme-ultraviolet (EUV) channels during an M1.9 flare that occurred on 2011 September 23–24. The nonthermal HXR emission in 25–50 keV observed by *RHESSI* shows five distinct impulsive peaks of decaying amplitude with a period of about 3 minutes. A similar QPP was observed in the microwave emission recorded by the Nobeyama Radioheliograph and Polarimeter in the 2, 3.75, 9.4, and 17 GHz channels. Interestingly, the 3-minute QPP was also observed in the metric and decimetric radio frequencies (25–180, 245, 610 MHz) as repetitive type III bursts. Multiwavelength observations from the *Solar Dynamics Observatory*/Atmospheric Image Assembly, *Hinode*/SOT, and *Solar TERrestrial RELations Observatory*/SECCHI suggest a fan-spine topology at the eruption site, associated with the formation of a quasi-circular ribbon during the flare. A small filament was observed below the fan loops before the flare onset. The filament rose slowly and interacted with the ambient field. This behavior was followed by an untwisting motion of the filament. Two different structures of the filament showed an approximately 3-minute periodic alternate rotation in the clockwise and counterclockwise directions. The 3-minute QPP was found to highly correlate with 3-minute oscillations in a nearby sunspot. We suggest that the periodic reconnection (modulated either by a sunspot slow-mode wave or by an untwisting filament) at a magnetic null point most likely causes the repetitive particle acceleration, generating the QPP observed in HXR, microwave, and type III radio bursts.

Key words: magnetic fields – Sun: corona – Sun: filaments, prominences – Sun: flares – Sun: oscillations – sunspots

Supporting material: animations

1. INTRODUCTION

Quasiperiodic pulsations (QPPs) with periods from a few seconds to several minutes are often observed during solar flares in X-ray, radio, and optical wavelength bands (e.g., Aschwanden 2004; Nakariakov & Melnikov 2009; Nakariakov et al. 2010). Similar QPPs have also been detected in stellar flares (e.g., Mathioudakis et al. 2003; Pandey & Srivastava 2009; Anfinogentov et al. 2013; Balona et al. 2015; Pugh et al. 2015). The study of the QPP phenomenon is promising in the context of understanding the basic physics of flaring energy releases and charged particle acceleration and for the indirect estimation of plasma parameters by the method of magnetohydrodynamic (MHD) seismology (e.g., Roberts 2000; De Moortel & Nakariakov 2012; Liu & Ofman 2014).

The production of QPPs in flares may be associated with several physical mechanisms associated with flares. The following mechanisms could be responsible for the QPP formation:

(1) QPPs may be associated with a periodic, bursty regime of spontaneous magnetic reconnection, such as by the tearing of the current sheet associated with the formation of multiple plasmoids (Kliem et al. 2000). The coalescence and interaction of different plasmoids moving up and down along the flaring current sheet can periodically modulate the bidirectional (up and down) acceleration of electrons (Bárta et al. 2007, 2008). In this case, drifting pulsating structures (DPSSs) in the decimetric radio frequencies are expected to be observed

(Karlický et al. 2010). Recently, multiple plasmoids moving bidirectionally along an apparent current sheet have been observed in the extreme ultraviolet (EUV) (Takasao et al. 2012). Simultaneous observations of multiple plasmoids and DPSSs (for a duration of ~ 1 minute) have been recently reported by Kumar & Cho (2013). Therefore, tearing of the current sheet and the formation of multiple plasmoids can generate QPPs in the radio and hard X-ray (HXR) with periods from seconds to several minutes.

(2) The coalescence of current-carrying coronal loops can result in periodic variation of the coalescence current sheet width, accompanied by periodic production of nonthermal electrons. It would generate QPPs in the HXR and radio bands (Tajima et al. 1987; Kumar et al. 2010). In particular, the 25–48 s QPPs detected in the rising phase of solar flares were associated with this mechanism by Fárník et al. (2003).

(3) In the model recently proposed by Takasao et al. (2015), numerical simulations of the shock formation and evolution of the thermal structure in and above postflare loops demonstrated that the strength of the termination shock shows a quasiperiodic oscillation. This scenario can also be classified as a spontaneously generated QPP.

(4) The interaction of MHD waves (e.g., fast-mode wave, slow-mode wave, or torsional Alfvén waves) with the reconnection site may lead to induced QPPs. Ning et al. (2004) studied recurrent explosive events with a period of ~ 3 –5 minutes and suggested that their triggering could be

caused by an MHD wave. A fast-mode MHD wave model proposed by Nakariakov et al. (2006) links the triggering of QPP with a transverse oscillation of a coronal loop situated near the reconnection region or current sheet. Doyle et al. (2006) studied the repetitive occurrence of explosive events at a coronal hole boundary and suggested a periodic triggering of reconnection by a kink oscillation of the flux tubes in the closed-field-line region. Chen & Priest (2006) modeled explosive events in the transition region and showed that the repetitive reconnection (e.g., with a period of 3–5 minutes) could be triggered by a slow-mode MHD wave. This idea was further developed by Sych et al. (2009), who demonstrated that 3-minute QPPs observed during a flare could be triggered by the along-the-field leakage of 3-minute slow-mode oscillations in the umbra of a nearby sunspot. In two-ribbon flares, repetitive reflection of flare-excited slow-mode waves from footpoints of the flaring arcade may also be a possible mechanism for triggering the periodic reconnection (Nakariakov & Zimovets 2011). In that scenario, the HXR source moves with a subsonic and sub-Alfvénic speed along the neutral line, which is consistent with observations.

Despite significant progress in both theoretical modeling and observational detection, the specific mechanisms for the QPPs observed in solar and stellar flares are still not well understood and need further investigations. In particular, an analysis of QPPs in high-resolution multiwavelength observations (e.g., simultaneously in EUV, X-ray, and radio) can provide a more complete picture of the flare event and allow us to draw important conclusions on the QPP generation mechanisms.

Recently, Kumar et al. (2015) studied a decaying QPP with the period of about 202 s in the 6–12 keV X-ray and EUV channels. They found that the QPP was generated by periodic reconnection caused by an untwisting small filament at a three-dimensional (3D) null point in a fan-spine magnetic topology. Energetic particles accelerated along the arcade loops toward the opposite footpoints and precipitated there were associated with periodic EUV brightening. Apart from the 202 s QPP, a 409 s oscillation was also observed as a periodic alternate flow along the arcade loops and was interpreted as a slow-mode (longitudinal) wave excited by a flare triggered at one of the footpoints of the arcade loops.

In this paper, we analyze a QPP observed in HXR (25–50 keV), microwave (17 GHz), and EUV emission in an M1.9 flare on 2011 September 23–24. The flare exhibits a quasi-circular ribbon, which suggests the possible magnetic configuration to be a fan-spine topology at the boundary of the active region (AR) NOAA 11302. In Section 2, we present the observations and results. In the last section, we summarize and discuss our results.

2. OBSERVATIONS AND RESULTS

The *Atmospheric Image Assembly* (AIA; Lemen et al. 2012) on board the *Solar Dynamics Observatory* (SDO; Pesnell et al. 2012) captures full-disk images of the Sun in a field of view of about $1.3 R_{\odot}$, a spatial resolution of $1''.5$ ($0''.6 \text{ pixel}^{-1}$), and a time cadence of 12 s in 10 EUV and UV channels. The present study utilizes 171 Å (Fe IX, corresponding to the temperature T of about 0.7 MK), 94 Å (Fe XVIII, $T \approx 6.3$ MK), 131 Å (Fe VIII, Fe XXI, Fe XXIII, i.e., $T \approx 0.4$, 10 and 16 MK, respectively), 304 Å (He II, $T \approx 0.05$ MK), and 1600 Å (C IV + continuum, $T \approx 0.1$ MK and 5000 K) images. We also used Heliospheric and Magnetic Imager (HMI) magnetograms

(Schou et al. 2012) to investigate the magnetic configuration of the AR. We used *RHESSI* (Lin et al. 2002) HXR and Nobeyama Radioheliograph (NoRH; Nakajima et al. 1994) and Polarimeter (NoRP; Nakajima et al. 1985) observations to determine the HXR and microwave source location of the observed QPP.

The AR NOAA 11302 was located near the eastern limb (N12E56) on 2011 September 23, with a $\beta\gamma$ magnetic configuration. The QPP reported here was observed during an M1.9 flare. The flare was triggered at the edge of the AR, where the fan-shaped loops were observed within the preexisting active region. The flare started at $\sim 23:48$ UT, peaked at $\sim 23:56$ UT, and ended at $\sim 00:04$ UT.

2.1. Quasiperiodic Pulsation

Figure 1(a) displays the *GOES* soft X-ray flux profile (3 s cadence) in the 1–8 Å channel and its derivative (red curve) estimated by using the three-point Lagrangian interpolation method. Interestingly, the time derivative of the flux profile reveals a clear QPP. Figure 1(b) shows *RHESSI* HXR count rate time profiles (4 s cadence) in the 12–25 keV (black), 25–50 keV (blue), and 50–100 (red) keV channels. The decaying oscillation is especially clear in the 25–50 keV channel. Five distinct bursts of the energy release are labeled 1 through 5. The 50–100 keV flux profile shows only the first two bursts of the energy release, while the other three bursts are not detected in this energy range. To investigate the QPP in radio channels, we plotted NoRP (1 s cadence) flux profiles in the 2, 3.75, 9.4, and 17 GHz channels (Figure 1(c)). We can see a clear QPP cotemporal with the *RHESSI* HXR bursts.

Figure 1(d) displays the dynamic radio spectrum in 25–180 MHz frequency observed at the Learmonth radio observatory, Australia. We can see a series of quasiperiodic type III radio bursts during the flare. We also used Radio Solar Telescope Network (RSTN) 1 s cadence data from the Learmonth observatory to see the radio flux density profiles in the 245, 610, 8800, and 15,400 MHz frequency bands (Figures 1(d)–(h)). The QPP is clear in all of the light curves, not only in the high-frequency radio bursts (2, 9.4, 17 GHz) but also in the low-frequency (245, 610 MHz) channels.

Nonthermal electrons responsible for the HXR and microwave emissions may be accelerated by the same process during the flare, e.g., magnetic reconnection (Kundu 1961, 1965), but have different energies (Kai 1986). The footpoint HXR emission is generated during the precipitation of the nonthermal electrons with energies of tens of kiloelectronvolts, whereas the microwave emission is produced by trapped nonthermal electrons of several hundreds of kiloelectronvolts (Kundu et al. 1994; White et al. 2003; Asai et al. 2013). Spatially, the microwave emission comes from the body of the flaring loop, while the HXR emission comes from its footpoints and loop top. Therefore, microwave and HXR emissions are generated by the nonthermal electrons accelerated in the reconnection site and precipitated or transported downward into the chromosphere. In contrast, the 25–180 and 245 MHz channels show quasiperiodic type III radio bursts excited by the nonthermal electrons propagating upward (along the open field lines) from the reconnection site to the interplanetary medium. The emission at the decimetric frequency (e.g., 610 MHz) is generally associated with the acceleration region (Aschwanden & Benz 1997; Aschwanden 2004). Type III radio bursts above 1 GHz are

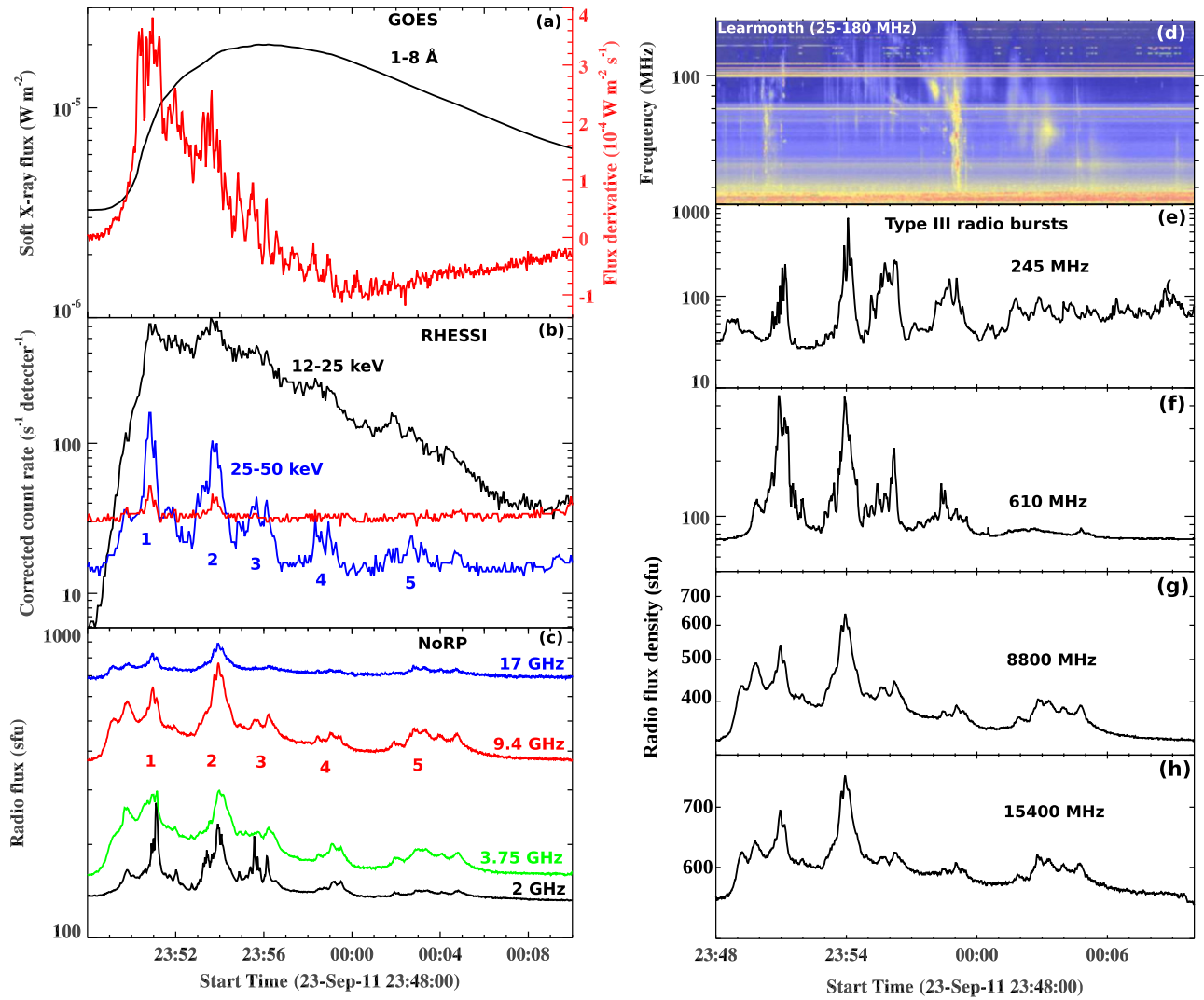


Figure 1. (a) *GOES* soft X-ray flux profile in the 1–8 Å channel and its time derivative (red). (b) *RHESSI* hard X-ray flux profiles in the 12–25, 25–50, and 50–100 keV channels. (c) NoRP flux profiles in the 2, 3.75, 9.4, and 17 GHz frequency bands. (d) Learmonth dynamic radio spectrum in 25–180 MHz frequency, showing bunches of type III radio bursts. (e)–(h) RSTN radio flux density profiles in 245, 610, 8800, and 15,400 MHz frequencies from the Learmonth solar observatory.

generated by the electron beams propagating downward from the acceleration site (Bastian et al. 1998). We observed an approximately 3-minute periodicity in type III radio bursts (below 300 MHz), microwave bursts (above 1 GHz), and HXR bursts (25–50 keV) simultaneously, which therefore indicates the bidirectional acceleration and injection of electrons (Aschwanden & Benz 1997) from the acceleration region. Thus, this event suggests the quasiperiodic acceleration of electrons, which then propagate from the reconnection site upward and downward, bidirectionally.

Although the oscillatory pattern is clear in all the original light curves, we used the Lomb–Scargle periodogram method (e.g., Scargle 1982; Horne & Baliunas 1986) for the determination of the oscillation period and its confidence level. Figure 2(a), (b) shows the results of the periodogram analysis (i.e., the power spectra) for the 25–50 keV *RHESSI* HXR signal (4 s cadence) and RSTN 15.4 GHz radio signal (1 s cadence). The confidence level of 99% is marked by the horizontal dashed line. A period of approximately 3 minutes (above the 99% confidence level) is revealed in both the *RHESSI* and microwave signals. We would like to stress that the confidence levels shown in the power

spectra correspond to the highest spectral peaks only and cannot be used for the determination of the significance of the secondary peaks. We also applied Morlet wavelet analysis (Torrence & Compo 1998) on the *RHESSI* and NoRH light curves. The resultant wavelet power spectra are shown in Figures 2(c), (d). Again, the 3-minute periodicity is seen to be significant in both of the wavelet spectra above the 99% confidence level, which is consistent with the periodogram analysis.

We generated the X-ray spectrum obtained with *RHESSI* during 23:53–23:54 UT using the OSPEX package in SolarSoft (SSWIDL) (Figure 3). The background-subtracted photon flux is fitted with thermal (green) and nonthermal (yellow) components. We used an isothermal component (V_{th}) for the optically thin thermal bremsstrahlung radiation and a thick-target bremsstrahlung version-2 model (thick2) for the nonthermal photon flux that is due to the interaction of accelerated electrons with the thick-target plasma. We chose the 6–50 keV energy range, indicated by vertical dotted lines, for fitting purposes. From the best-fitting parameters, we derived the temperature T and emission measure of the hot plasma to be 14.8 MK and $0.68 \times 10^{49} \text{ cm}^{-3}$, respectively.

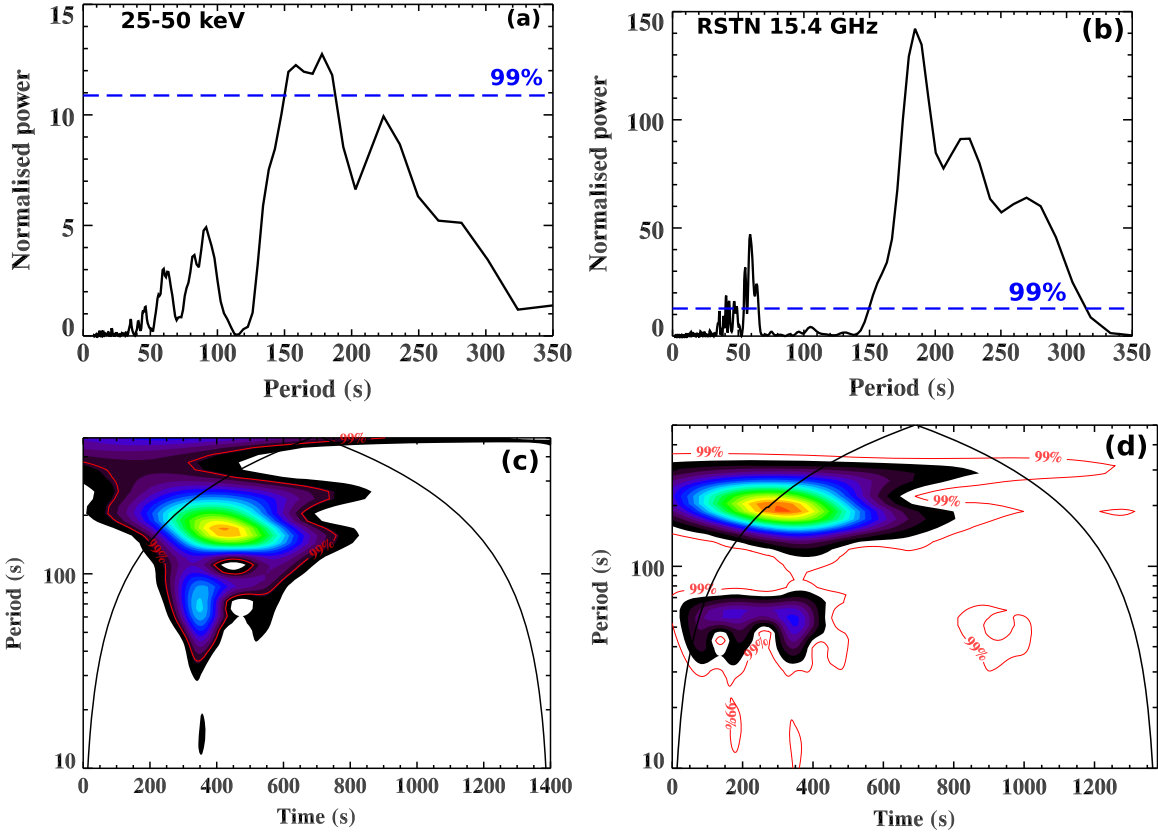


Figure 2. (a)–(b) Lomb–Scargle periodograms of *RHESSI* 25–50 keV and RSTN 15.4 GHz signals. (c)–(d) Wavelet power spectra for *RHESSI* 25–50 keV energy channel (left) and RSTN 15.4 GHz (right) signals. The start time is 23:48 UT.

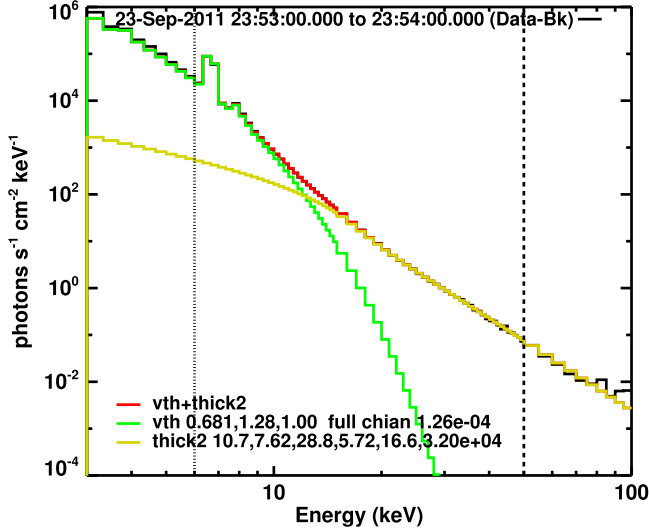


Figure 3. *RHESSI* energy spectrum fitted with the isothermal (green) and thick-target bremsstrahlung (yellow) models for the interval 23:53–23:54 UT.

The spectral index for the thick-target bremsstrahlung is 7.6. The nonthermal component dominates over the thermal component above ~ 13 keV. Therefore, it is clear that the observed QPP is basically related to the periodic variation of the nonthermal electron flux.

2.2. Spatial Location of the Hard X-Ray and Radio Sources

To investigate the particle precipitation or transport sites during the flare, we used HXR 25–50 keV and NoRH

17/34 GHz images. We chose the Pixion algorithm (Metcalf et al. 1996) for the *RHESSI* image reconstruction. The Pixion method is considered to be the most accurate algorithm (Hurford et al. 2002). The integration time for each image was 20 s. We utilized NoRH 5 s cadence intensity images (R+L) at 17 and 34 GHz. Figure 4 displays the HXR 25–50 keV (blue) and NoRH 17 GHz (red) contours overlaid on the AIA 1600 Å images at $\sim 23:51$ UT. These images are used at the peak time of each of the bursts observed in the HXR 25–50 keV and microwave channels. Figure 4(a) shows a small filament rising at the flare site. We can easily identify the two legs of the filament (marked by N and S in the figure). Generally, the filaments are observed in the chromospheric images (e.g., H α and AIA 304 Å). However, if the kink-unstable filament is heated during magnetic reconnection, it is often observed in the AIA 1600 Å channels (e.g., Kumar et al. 2012 and Kumar & Cho 2014). The locations of both the 25–50 keV sources and the 17 GHz source are almost at the quasi-circular ribbon. However, their centroids constructed at the 90% level of the peak intensity are not cospatial. We note that the 25–50 keV sources (centroid) are located close to the legs of the filament, whereas the 17 GHz source is located at the footpoints of an underlying flare loop. To identify the location of the flare loop, we selected the AIA 94 Å hot channel image at 23:53 UT. In this image (panel b), we show the NoRH 34 GHz contours (yellow) overlaid on AIA 94 Å images at $\sim 23:53$ UT. This is done to show the coronal loops associated with the eruption of the small filament. The overlying 34 GHz source is cospatial with the small loop located above the quasi-circular ribbon. This 34 GHz emission

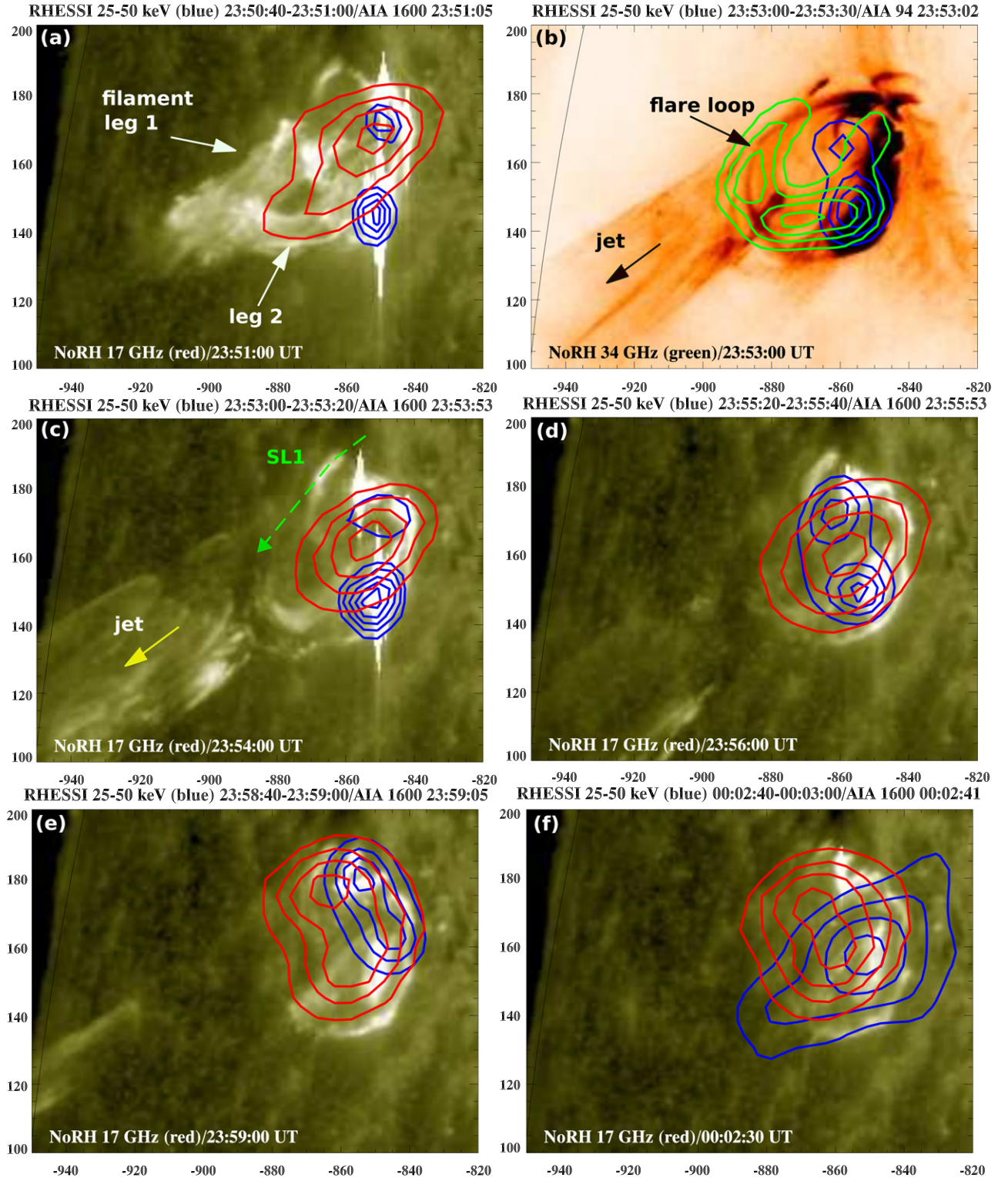


Figure 4. *RHESSI* hard X-ray (25–50 keV, blue) and NoRH (R+L) 17 GHz sources shown by the contours overlaid on the AIA 1600 Å images. Panel (b) shows *RHESSI* 25–50 keV (blue) and NoRH 34 GHz (green) contours over the AIA 94 Å negative image. The time of each image matches the peak time of the 3-minute oscillation in the hard X-ray 25–50 keV and radio 17 GHz. The contour levels are 30%, 50%, 70%, and 90% of the peak flux. We included an extra contour level (i.e., 10% of the peak flux in panel (c)) to show the opposite footpoint of the loop. The axes are labeled in arcsecs.

may be the evidence of trapped nonthermal electrons in the loop. The rising filament is heated during reconnection with the ambient fields and then decays into an untwisting jet, as seen in Figures 4(b)–(e). Furthermore, during ~23:53–23:59 UT, we see the footpoint HXR sources. The NoRH 17 GHz sources

cover the quasi-circular ribbon (Figures 4(c)–(d)) and could be the emission from the trapped electrons in the loop. This suggests that the bursts are most likely caused by the same population of nonthermal electrons with different energies.

2.3. Magnetic Configuration

To investigate the magnetic configuration of the flare site, we used *Hinode*/SOT (Tsuneta et al. 2008), XRT (Golub et al. 2007), *SDO*/HMI, and AIA images. Figures 5(a), (b) display HMI magnetograms of the flaring active region on 2011 September 24 (left) and September 25 (right). Since the active region was close to the eastern limb, some of the magnetic polarities at the edge of a big sunspot may not be true. We carefully checked the magnetic polarities after September 24, when the active region was closer to the disk center. At the flare site, we observe negative polarities (N) surrounded by the positive-polarity region (three sides). The arc-shaped polarity inversion line (PIL) is marked by the green line. The M-class flare occurred at the edge of the active region. The Ca II H line images (Figures 5(c), (d)) show a quasi-circular flare ribbon. Circular or quasi-circular flare ribbons generally indicate the presence of a fan-spine topology at the flare site (Masson et al. 2009; Pariat et al. 2010; Wang & Liu 2012; Cheung et al. 2015; Kumar et al. 2015). We also noticed the presence of bright upflows along the possible spine (marked by the dotted line) in the chromosphere. Figure 5(e) displays the *Hinode* XRT image (Be_{thin}, $\log T \sim 6.8\text{--}7.0$ MK) during the flare onset (23:50:56 UT). Interestingly, we see quasi-circular brightening at the footpoints of the loops. The AIA 304 Å image (Figure 5(f)) shows a small filament lying along the neutral line. The AIA 171 Å image reveals open field lines with a possible fan-spine topology at the eruption site (Figure 5(g)). These images are overlaid by the HMI magnetogram contours of positive (red) and negative (blue) polarities.

The *Solar TERrestrial Relations Observatory* (STEREO) SECCHI-B (behind, Wuelser et al. 2004; Howard et al. 2008) observed the same active region close to the disk center. Therefore, it provides an opportunity to visualize the 3D structure of the active region loops. Also, SECCHI observed the flare and jet-like eruption of the filament material along the open field lines. Figure 6(a) displays the active region in the 171 Å channel before the flare onset (at 22:14:54 UT). We can see the fine structure and connectivity highlighted by different loops within the active region. We assume fan loops with an outer spine at the flare site. On the basis of these observations, we draw (over the image) open field lines and an outer spine at the eruption site. In Figure 6(b), we display the SECCHI 195 Å image showing the flare and associated plasma flow along the outer spine at 00:06:25 UT. Similar fan loops and the plasma motion along the outer spine were observed in the SECCHI 304 Å (reverse color) image (00:07:09 UT). The schematic cartoon of the fan-spine topology, including a possible 3D null point, is shown in Figure 6(c). The development of the filament resulted in an eruption that followed the open field line along the outer spine and produced a coronal mass ejection (CME) in the interplanetary medium.

2.4. Trigger of the Oscillation

Figure 7 displays several selected images taken in the AIA 131 Å channel. The 131 Å channel is sensitive to both hot ($T \approx 10$ MK) and cool plasma ($T \approx 0.4$ MK). Before the flare, we see a small filament (at $\sim 23:48$ UT) lying below the fan loops. The flare brightening starts with the rise of the filament (at 23:49:21 UT). The filament interacted with the overlying preexisting fields. The ejection of the filament is similar to the

blowout jet scenario (e.g., Moore et al. 2015). The filament material showed an untwisting motion during the eruption. We also noticed a transverse oscillation of a small loop above the flare center (Figure 7(f)).

To study the untwisting motion of the erupting filament, its speed, the kink oscillation of the small loop, and the associated downflows along the spine at the flare site, we used slice cuts S1, S2, S3, S4, and S5 made in the AIA 304, 171, 94, and 1600 Å images (Figure 8). Figures 8(a), (b) show the filament material ejected from the flare site in the AIA 304 Å intensity and 171 Å running-difference images. Cut S1 is used to detect the untwisting or rotation of the filament material, whereas cut S2 is used to visualize the outward plasma ejections during the periodic energy release. The direction of the slice cut is marked by the arrowhead at the end of the slice. Figure 8(c) shows the AIA 94 Å intensity image for the slice cut S3. Cuts S4 and S5 in the AIA 1600 Å (running-difference) image are used to detect the plasma downflows along the spine (Figure 8(d)).

Figures 9(a), (b) display the stack (running-difference intensity) plots along the slice S1 using sets of the AIA 304 and 171 Å images. We see the periodic brightening in these plots, which may be associated with the untwisting motion of the filament plasma. The bright propagating features in the stack plot show the tangential motion of the plasma. To see the temporal association of these untwisting motions with the periodic energy releases, we overplotted the *RHESSI* HXR flux (25–50 keV, blue curve) in panel (a). Interestingly, we see a good temporal correlation of the untwisting motion with the HXR bursts with a 3-minute period. The periodic brightening has an approximately 3-minute period, similar to the HXR emission. The linear/tangential speeds of untwisting features 2, 3, and 4 (blue dotted lines) are ~ 256 , ~ 235 , and ~ 130 km s⁻¹, respectively. The average speed is ~ 207 km s⁻¹. A careful investigation of Figure 9(b) reveals additional cotemporal untwisting motions in the bottom side of the stack plots. It is clear that the upper part (U) of the jet shows a counterclockwise motion, whereas the lower part (L) of the jet reveals a clockwise rotation. These oppositely directed untwisting motions may be a signature of a torsional Alfvén wave embedded in the filament material.

Figure 9(c) shows the erupting plasma motion along slice S2. The projected speed of the outward-moving plasma was ~ 632 km s⁻¹. Note that there are five distinct ejections. After interacting with the overlying fields, the filament showed impulsive acceleration.

In Figure 9(d), we display the stack plot along the slice S3 using 94 Å intensity images. It shows that the filament rise was followed by a transverse oscillation of the small loop located above the flare center. To see the association of the kink oscillation with the observed periodic particle acceleration, we determine the oscillation period to be $\sim 230 \pm 10$ s (i.e., about 4 minutes). The oscillation period is not consistent with the period of the detected QPP in the energy release. Therefore, it is unlikely that this kink oscillation of the small loop could trigger the periodic reconnection. The oscillations were observed mainly in the loop leg where we noted the downflows along the vertical spine field observed in the AIA 1600 Å. It seems that the loop oscillation is triggered by the unstable filament.

To see the quasiperiodic energy release and associated downflows in the EUV, we used AIA 1600 Å images. Figure 9(e) shows the mean 1600 Å intensity obtained by averaging the signals of individual pixels in a box that covers

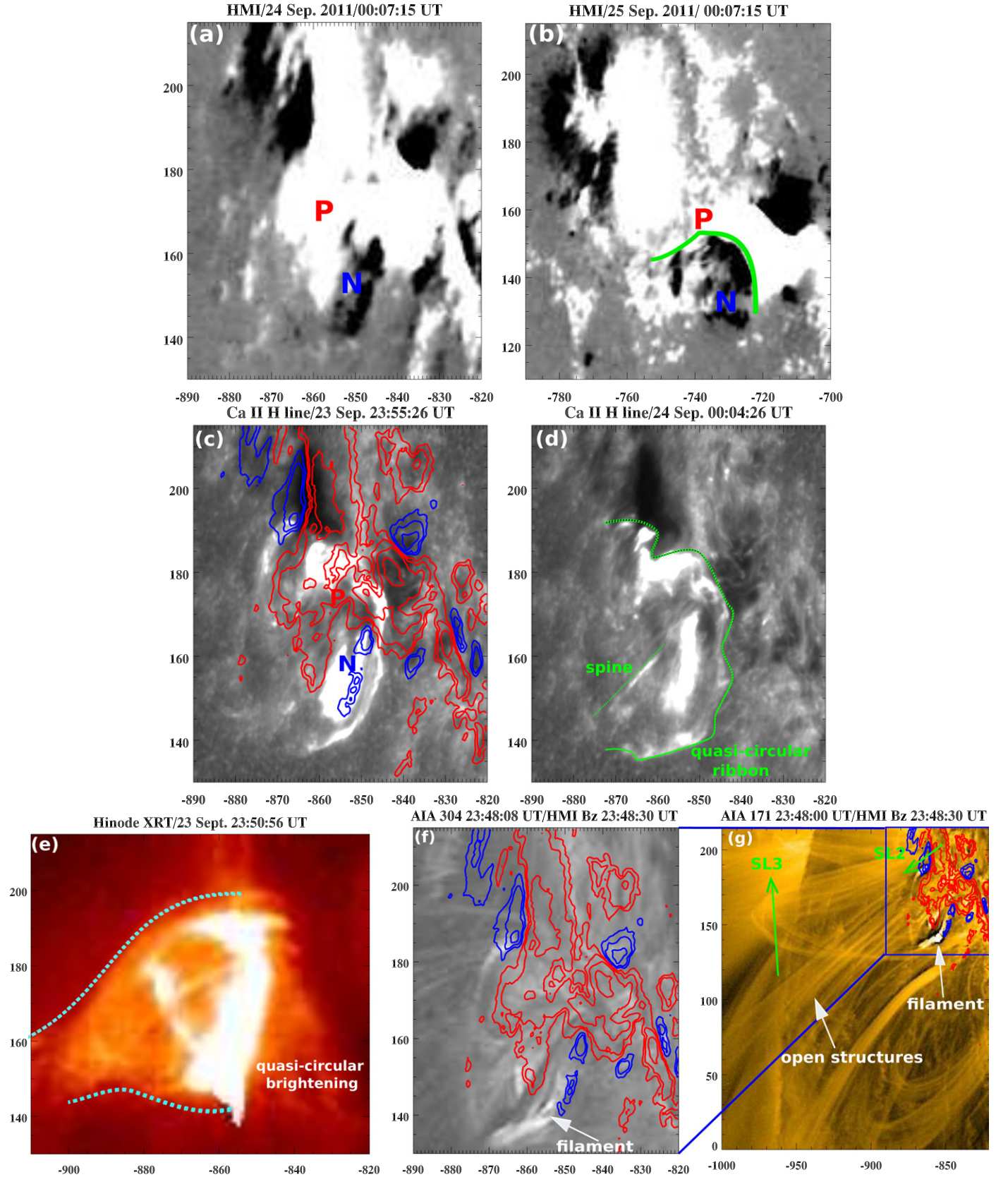


Figure 5. (a)–(b) HMI magnetogram of the flaring AR on 2011 September 24 and 25. P and N indicate positive and negative polarity fields. The green line is the PIL. (c)–(d) *Hinode*/SOT Ca II H line (3968 Å) images showing the flare ribbon morphology. (e)–(g) XRT image (Be_{thin} filter) during the flare onset showing the magnetic configuration and formation of quasi-circular brightening at the footpoints of the loops. The AIA 304 and 171 Å images are overlaid by an HMI magnetogram of positive (red) and negative (blue) polarities. The contour levels are ± 200 , ± 400 , ± 800 , and ± 1600 G.

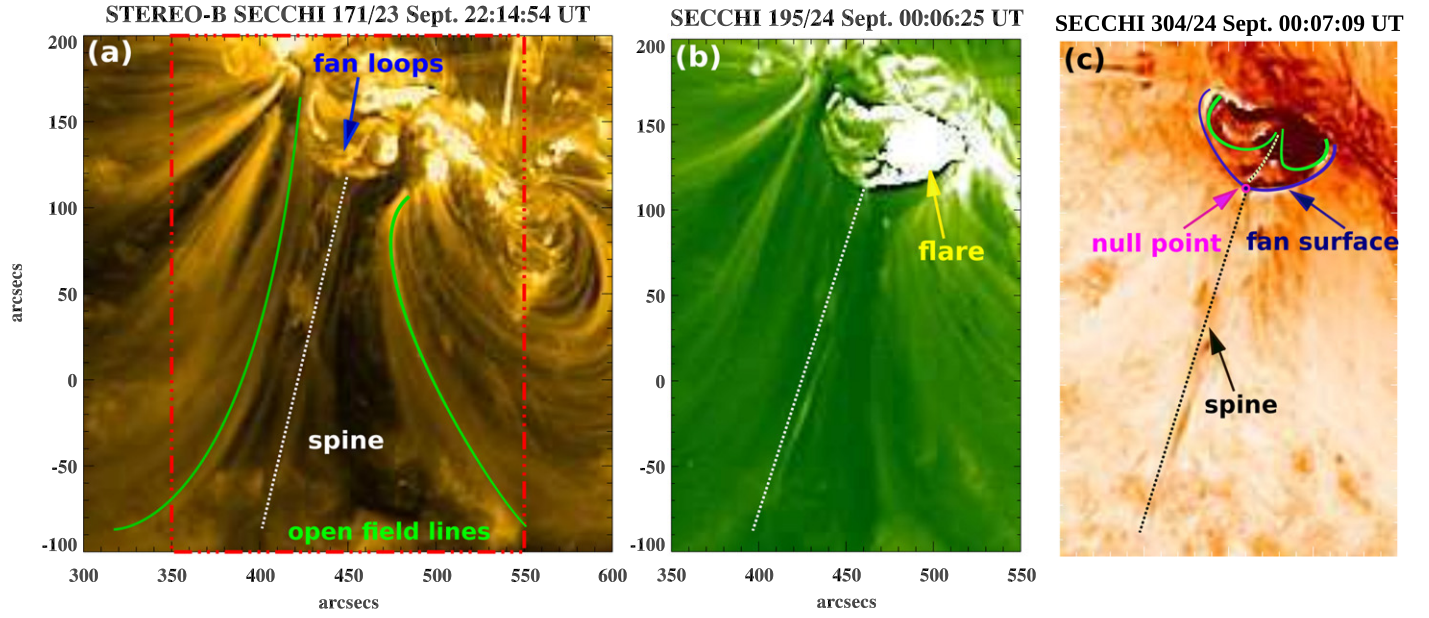


Figure 6. *STEREO-B* SECCHI intensity images in the 171, 195, and 304 (reverse color) Å channels. These images display the possible magnetic configuration (i.e., fan-spine topology) of the flare site. The rectangular box in panel (a) indicates the location of the field of view in panels (b) and (c).

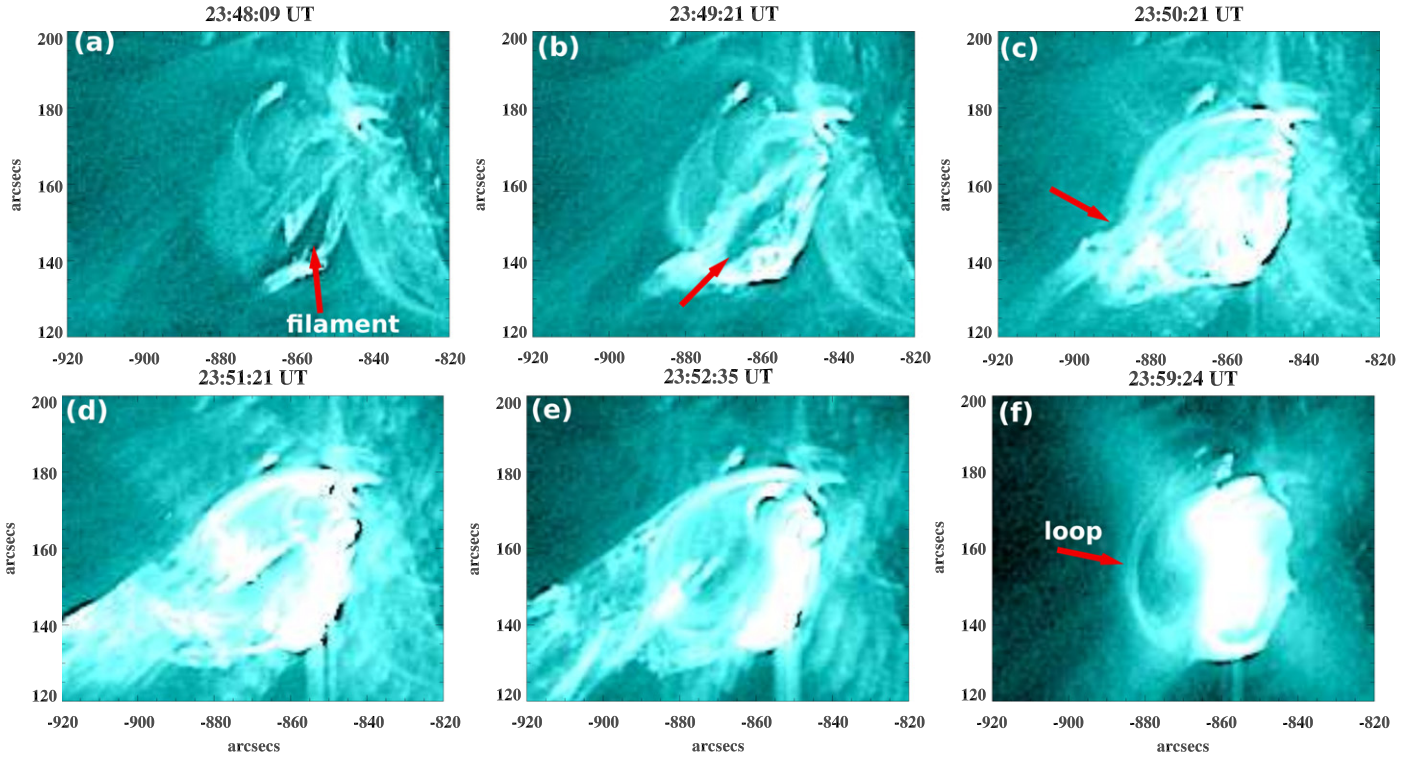


Figure 7. Selected AIA 131 Å images showing the filament rise, its interaction with the preexisting field, and associated plasma heating. (An animation of this figure is available.)

the flare ribbon. The quasiperiodic energy release observed in this channel is quite similar to the HXR emission (25–50 keV). The emission observed in the AIA 1600 Å channel is basically generated by the periodic precipitation of the nonthermal electrons propagating downward from the reconnection site. The periodic downflows are also observed along the spine (Figure 9(f)). The speed of these downflows is ~ 60 , ~ 84 , and ~ 52 km s $^{-1}$, respectively. The lower end of slice S5 covers a

sunspot north of the flare ribbon. The running-difference intensity plot clearly shows the periodic variation of the intensity (between the horizontal red dotted lines) generated by the precipitation of energetic particles. The variation of the average intensity between the red dotted horizontal lines is overplotted in panel (g). This finding indicates that leakage of sunspot oscillations could periodically trigger magnetic reconnection.

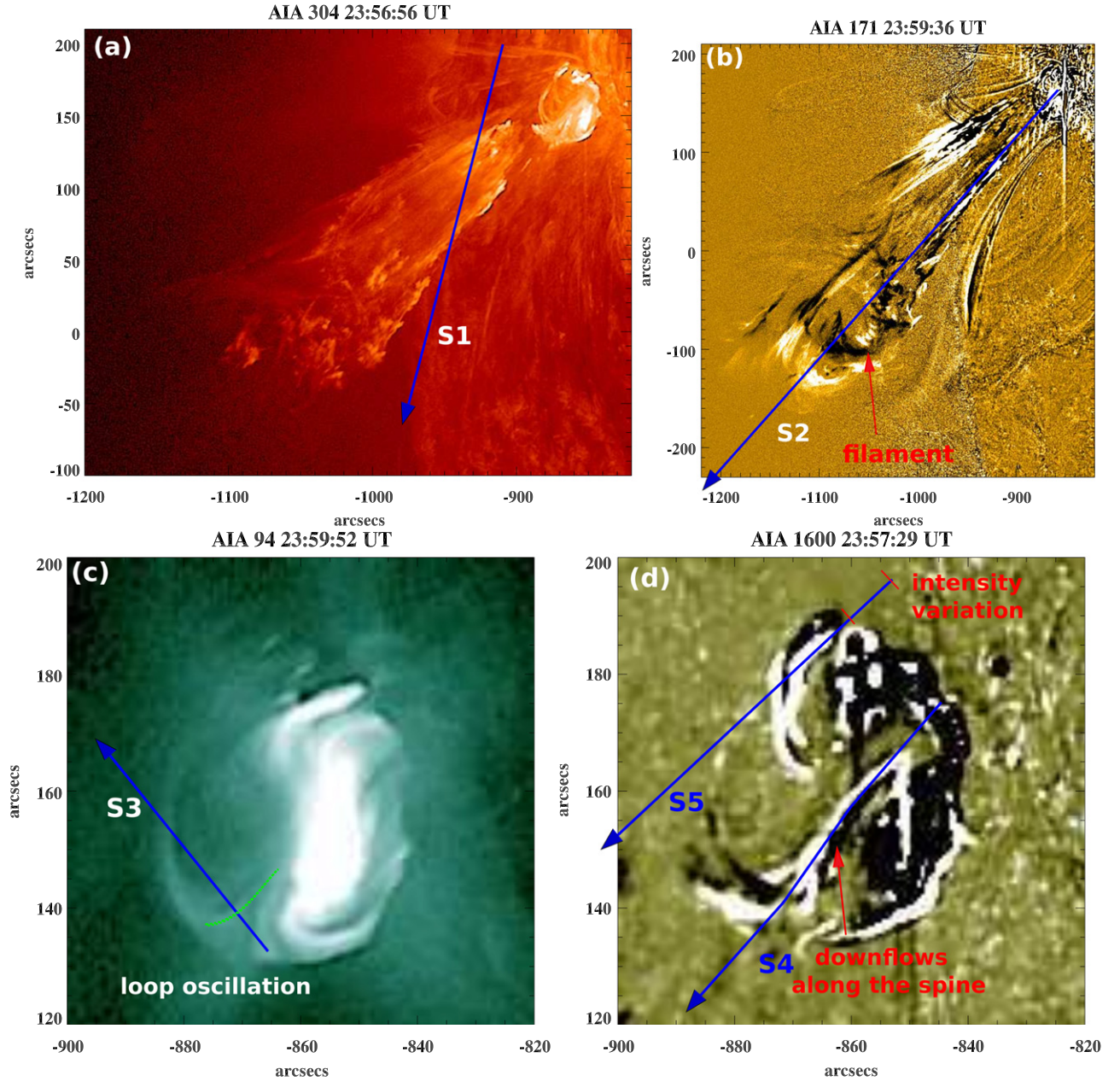


Figure 8. AIA 304, 171, 94, and 1600 Å images during the flare. S1, S2, S2, S4, and S5 are the slice cuts used to create the time–distance plots. The arrowhead indicates the direction of the cut for the time–distance plots.

(Animations (a, b, and c) of this figure are available.)

2.5. Wave Trains

In addition, in the AIA 171 Å channel we observed a rapidly propagating wave train. The AIA 171 Å running movie shows the wave train of the intensity variation during 00:06–00:18 UT, propagating in the southward direction. To determine the apparent speed of the wave train, we chose a curved path along the propagating wave train in the AIA 171 Å image (Figure 10(a)). Figure 10(b) displays the stack plot of running-difference intensity along the selected path. We see the propagating wave train starting at 00:06 UT. The individual wave fronts are labeled 1, 2, 3, 4, and 5. We chose the second wave front (blue dotted line) to determine the speed because this wave front was the most pronounced one. The average

projected speed of the front was found to be $\sim 320 \pm 27 \text{ km s}^{-1}$. The period of the filling signal in the wave train is ~ 2.2 minutes.

The speed of the individual fronts in the wave train is not as high as observed in the previous flares (Liu et al. 2012; Kumar & Manoharan 2013; Pascoe et al. 2013). The fast wave trains usually have higher speeds, $\sim 1000\text{--}2000 \text{ km s}^{-1}$, measured during the impulsive phase of a flare. In our case, we observed the wave train during the flare decay phase (00:06–00:18 UT). It is unclear why these wave trains are not observed during the flare impulsive phase. However, the estimated projected speed of the wave train in our case is consistent with the result of Liu et al. (2012), who observed lateral deceleration of a wave train from ~ 650 to 340 km s^{-1} .

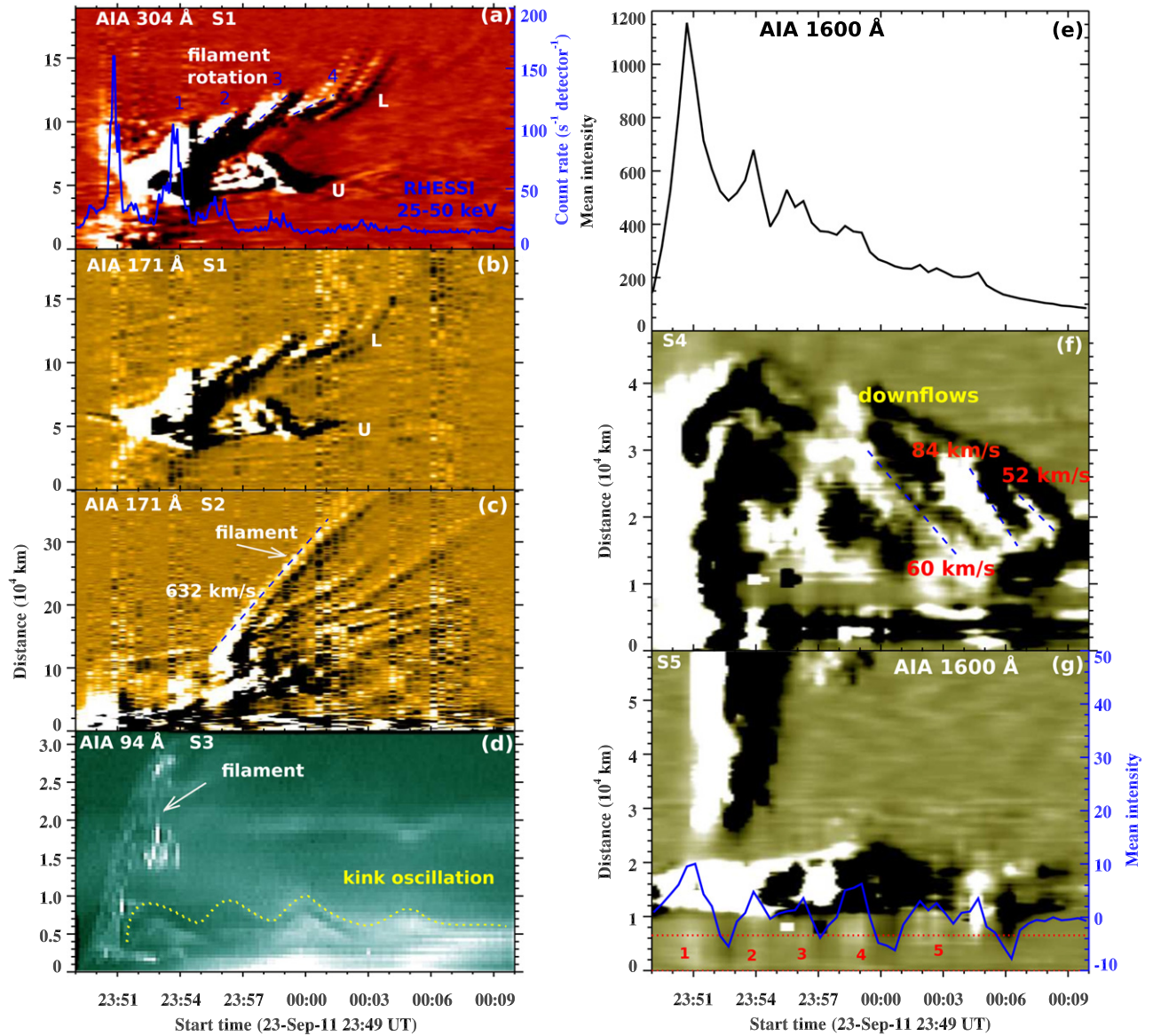


Figure 9. (a)–(d) Time–distance intensity plots along slices S1, S2, and S3 using AIA 304, 171, and 94 Å images. The AIA 304 and 171 Å plots are created from the running-difference images with the time of 1 minute between the images, while the AIA 94 Å plot is made from the intensity images. The blue curve is the *RHESSI* hard X-ray flux profile in the 25–50 keV channel. U and L are the upper and lower parts of the jet structure. (e) The AIA 1600 Å mean intensity profile extracted from box 1. (f)–(g) AIA 1600 Å time–distance running-difference intensity plots along the slices S4 and S5. The blue curve shows the mean intensity extracted between the two red horizontal dotted lines.

Let us assume that the wave train is generated during the periodic energy release. The time difference between the start time of the HXR burst and the appearance of the wave trains is ~ 15 minutes. The distance of the observed wave train from the flare energy release site is $\sim 300''$. Let us assume that the initial speed of the wave train equals the filament material speed of $\sim 632 \text{ km s}^{-1}$. The time taken by the wave train to reach the observed distance will be ~ 6 minutes. The estimated time is much smaller than the actual time difference from HXR bursts. Therefore it is unlikely that the wave trains are generated during the flare impulsive energy release.

2.6. Sunspot Oscillations and Kink Oscillations of the 171 Å Arcade Loops

To investigate the relationship between sunspot oscillations and the associated periodic energy release, we selected slices

SL1 and SL2 (AIA 1600 Å and 171 Å images shown in Figures 4(c) and 5(f)) at the sunspot located at the eruption site. The running-difference intensity along these cuts (SL1, SL2) during 23:32–00:18 UT is plotted in Figures 10(c), (d). The AIA 1600 Å movie reveals the repeated umbral flashes before the flare onset at 23:32 UT onward. Interestingly, we noticed the increase in the umbral intensity by the periodic precipitation of nonthermal electrons during the flare, which is cotemporal with the *RHESSI* HXR flux (25–50 keV, blue curve). Since the intensity change (marked in Figure 8(d)) is consistent with the AIA 1600 Å mean intensity profile and HXR profile, it is likely that the intensity change could be a result of particle precipitation near the sunspot. However, we also observed the leakage of the slow-mode waves cotemporally in the AIA 171 Å channel (Figure 10(d)).

Figure 10(d) shows the propagating EUV disturbances, going from the sunspot along slice SL2 (AIA 171 Å). Their

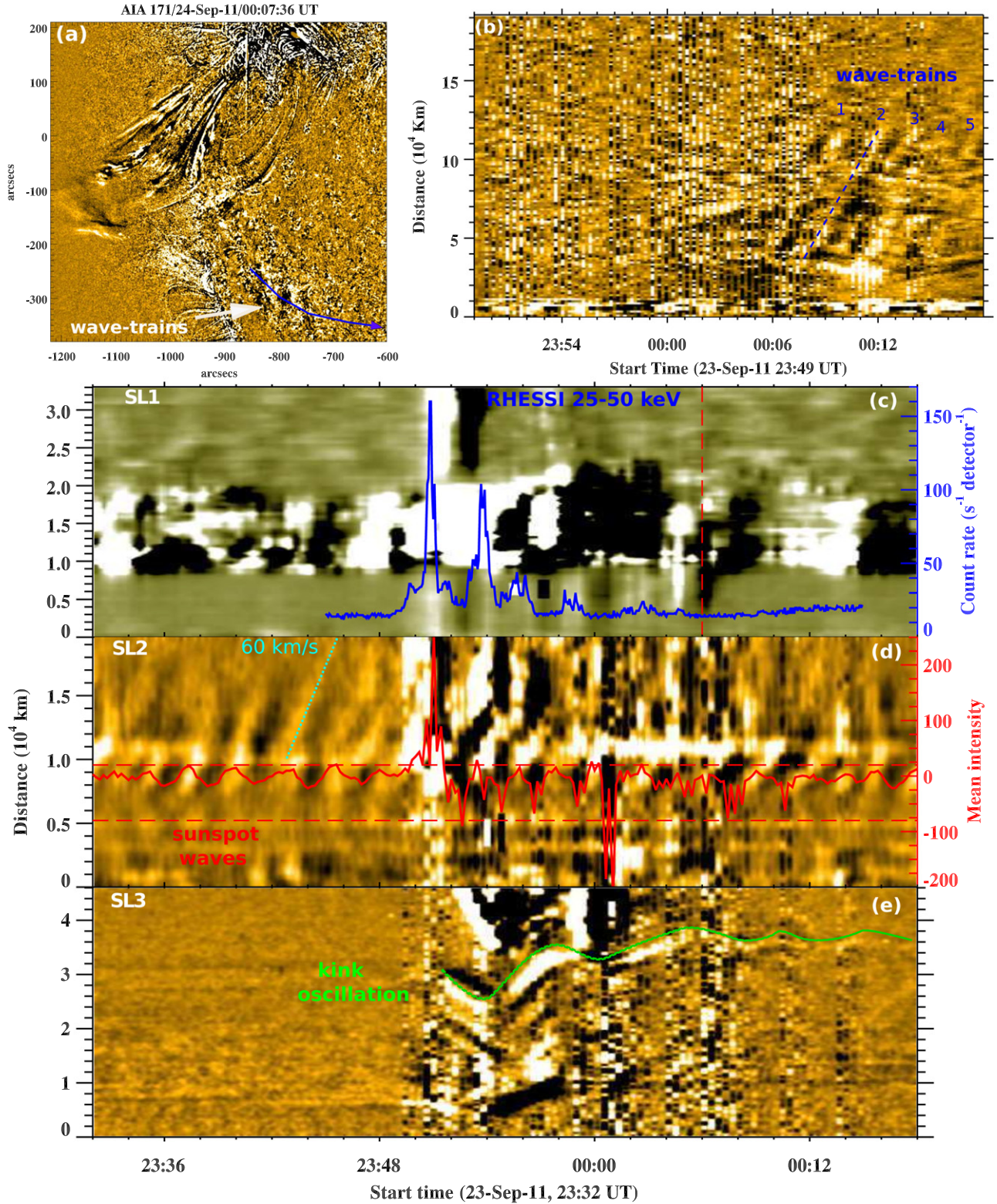


Figure 10. (a) AIA 171 Å running-difference image showing a rapidly propagating wave train. (b) Time-distance intensity (running-difference) plot along the selected path (blue) shown in panel (a). (c) Stack plot of the AIA 1600 Å running-difference intensity along slice SL1 shown in Figure 4(c). The blue curve is the *RHESSI* hard X-ray flux profile in the 25–50 keV channel. The vertical dotted line (red color) shows the appearance of the wave train in the AIA 171 Å channel. (d), (e) Stack plots of the AIA 171 Å running-difference intensity along the slices SL2 and SL3 (refer to Figure 5(f)) showing 3-minute waves leaking from a sunspot and the 6-minute kink oscillations (green) of the overlying arcade loops, respectively. The red curve shows the mean intensity extracted between the two horizontal lines shown in the middle panel.

(An animation of this figure is available.)

apparent (i.e., projected) speed is subsonic for the temperature associated with these EUV channels, so they are interpreted as slow magnetoacoustic waves (de Moortel 2009). In our case, the apparent speed of a front is $\sim 60 \text{ km s}^{-1}$ (Figure 10(d)). The average intensity (running difference) has been extracted from the 171 Å stack plot (between the two horizontal dashed lines) and overplotted in the same panel (red curve). A comparison of the timing of sunspot oscillations with the *RHESSI* HXR flux profile suggests a high correlation between them. Therefore, it is very likely that the reconnection is periodically modulated by the slow-mode waves leaking from the sunspot. The possible leakage of umbral oscillations in the corona along magnetic field lines in the form of slow-mode waves has been demonstrated in Botha et al. (2011). The slow-mode waves can reach the reconnection site in the fan-spine topology and periodically trigger the energy release by the mechanism described by Chen & Priest (2006) and Sych et al. (2009).

Furthermore, we also noticed a kink oscillation of the overlying arcade loops at the eruption site. Figure 10(e) shows the running-difference intensity plot along slice SL3 in the AIA 171 Å image (Figure 5(f)). During the first HXR burst, we see the contraction of the arcade loops followed by decaying kink oscillations. The oscillation period is ~ 6 minutes. The oscillation was possibly triggered by the erupting jet-like structure of the untwisting filament. Alternatively, the contraction of the cool arcade loops may be due to the decrease in the magnetic pressure at the flare site as a result of the magnetic energy release during the flare (Hudson 2000).

2.7. Coronal Mass Ejection

The jet-like eruption of the small filament produced a CME, which was observed during the event by the *SOHO*/LASCO coronagraph (Brueckner et al. 1995; Yashiro et al. 2004). The CME frontal loop appeared at 00:12:06 UT in the LASCO C2 field of view. The CME speed (from the LASCO CME catalog⁵) was $\sim 617 \text{ km s}^{-1}$, which is close to the filament material speed ($\sim 632 \text{ km s}^{-1}$) in the low corona (Figure 9(c)). The CME does not show significant deceleration (2.83 m s^{-2}) up to $\sim 20 R_{\odot}$ in the interplanetary medium.

3. SUMMARY AND DISCUSSION

We presented multiwavelength observations of a 3-minute QPP in a solar flare, detected simultaneously in the HXR, radio, and EUV channels. Recently, Kumar et al. (2015) observed a decaying oscillation in the flaring emission, with three distinct peaks in the X-ray (6–12 keV) channel observed by the Fermi Gamma-ray Burst Monitor. Here we observed decaying oscillations in the *RHESSI* HXR channel (25–50 keV) with five distinct peaks without any gradual broadening in the burst profile. The specific results of this study are summarized below:

(1) We observed a quasi-circular ribbon during the flare, which suggests a fan-spine magnetic topology of the flare site (see Masson et al. 2009; Pariat et al. 2010; Pontin et al. 2013; Kumar et al. 2015, for discussion). In Masson et al. (2009), the outer spine is connected to a remote ribbon. Nonthermal electrons are accelerated at the reconnection site and propagate downward along the fan loops and upward along the outer spine. A circular or quasi-circular ribbon is generated by the

precipitation of nonthermal electrons downward along the fan loops. If the outer spine is connected within the active region (i.e., closed), we should observe a remote ribbon as a result of confined electrons along the outer spine/arcade loops that precipitate at the opposite footpoint. The formation of a remote ribbon within the active region with a fan-spine topology suggests a closed spine (e.g., Masson et al. 2009; Kumar et al. 2015). If the outer spine is open (Pariat et al. 2010), we generally do not expect a remote ribbon associated with the outer spine. In addition, we should observe the type III radio bursts, suggesting the injection and escape of nonthermal electrons (into the interplanetary medium) along the open field lines. The HXR sources (25–50 keV) that we observe are close to the footpoints of the kinked filament and within or at the quasi-circular ribbon. We also observed open structures in the AIA 171 Å and *STEREO* images emanating from the flare site. A 3D model of solar jets with a fan-spine topology including a magnetic null and open outer spine is proposed by Pariat et al. (2010). Our case study does not show a remote ribbon (within the AR) associated with the outer spine. We only observed a quasi-circular ribbon and periodic type III radio bursts. Therefore, this indicates that the magnetic configuration (in our case) is most likely a fan-spine topology where the outer spine is open (similar to Pariat et al. 2010).

In addition, we noted the untwisting motion of a filament material with an almost 3-minute period. Therefore, the rising filament interacts with the overlying preexisting field and can periodically trigger magnetic reconnection at the null point, resulting in quasiperiodic injection of nonthermal electrons toward the footpoints of the fan loops, leading to the formation of quasi-circular ribbons.

(2) The presence of periodic type III radio bursts suggests the propagation of nonthermal electrons along the open field lines. This means that the outer spine is extended into the interplanetary medium (i.e., open field lines at the eruption site) and is not connected to the remote site within the active region, as was observed by Kumar et al. (2015). Note that Kumar et al. (2015) did not observe type III radio bursts in the interplanetary medium because of the possible confinement of the accelerated (nonthermal) electrons in the arcade loops (i.e., no escape into the interplanetary medium) within the active region. Moreover, the formation of a remote ribbon along with heating of the arcade loops (131 and 94 Å channels) suggests the precipitation of nonthermal electrons toward the opposite footpoint of the heated arcade loop, which produced a 3-minute EUV QPP similar to that observed in the X-ray channel. In addition, the oscillation event studied by Kumar et al. (2015) showed a failed eruption of an untwisting small filament that interacted with the fan-spine magnetic field configuration. The absence of longer, hot arcade loops that could be visible in the 131 and 94 Å channels in our event confirms that the particles are not accelerated or transported (along the closed spine/arcade loops) from the flaring footpoint to the opposite footpoint (i.e., remote ribbon) in the active region. Therefore, the magnetic topology is open, allowing it to produce periodic type III radio bursts. In addition, in this study we observed a successful eruption of a small filament leading to a CME observed by the LASCO C2 coronagraph.

(3) This event does not reveal a slow-mode wave propagating back and forth along the hot arcade loops, as reported by Kumar et al. (2013, 2015). Therefore, we can rule out the trigger of periodic reconnection by a slow-mode wave

⁵ http://cdaw.gsfc.nasa.gov/CME_list/UNIVERSAL/2011_09/htpng/20110924.001206.p108g.htm.html

reflecting back and forth between the footpoints of the hot arcade loops. In fact, the periodic reconnection may be induced by the untwisting motion of the small filament (not by a reflecting longitudinal wave in the hot arcade loops). The rising filament reconnects with the preexisting fields and then gets destroyed to form a jet-like structure.

(4) This study also highlights the origin of the blowout jets observed in the coronal holes, which generally reveal an untwisting motion during the eruption (Moore et al. 2015). However, the properties of the coronal hole blowout jets are quite similar to the active-region jets originating in the fan-spine topology. This untwisting motion is generally observed during the interaction of a kink-unstable flux rope with the preexisting ambient field. One leg of the flux rope can be detached as a result of a reconnection that leads to the unwinding or untwisting motion of the flux rope (Kumar et al. 2012, 2015; Kumar & Cho 2014).

(5) The observed 3-minute QPPs are most likely triggered by slow-mode waves leaking from a nearby sunspot. The waves may be guided by the legs of the untwisting filament and trigger periodic reconnection at the null point by the mechanism proposed in Chen & Priest (2006). We observed a good temporal correlation between the sunspot waves and the HXR QPP. A similar scenario of the leakage of sunspot oscillations in the corona and periodic triggering (modulation) of flaring energy release was discussed in Sych et al. (2009).

(6) We observed kink oscillations of a small loop (131 and 94 Å) at the flaring site, with a period of ~4 minutes. In addition, we also observed kink oscillations of the overlying arcade loops (period of ~6 minutes). The kink oscillation period does not match the period of the observed QPP (~3 minutes). Therefore, we can rule out the modulation of the periodic reconnection by the kink oscillation of the nearby loops and consider the kink oscillations as a response of the coronal fast-mode (kink) MHD resonators to the flaring energy release. However, the wave train observed in this event may be generated by the periodic magnetic reconnection.

(7) The eruption of a flux rope can launch Alfvén waves in the opposite direction (up and down) along the flux rope or filament and can generate a vortical motion at the footpoints in the photosphere (Longcope & Welsch 2000; Fan 2009). Signatures of the torsional Alfvén waves have been detected in the small flux rope structures observed in the interplanetary medium (Gosling et al. 2010). In addition to the previous findings, our case study shows an untwisting motion of the filament material with almost the same period (~3 minutes) as the observed QPP. Moreover, we also noticed rotations in the opposite directions of two structures in the same jet. Very recently, Lee et al. (2015) performed a numerical simulation of helical blowout jets in an emerging flux region. They found that (1) the untwisting motion had been a result of reconnection of the twisted emerging magnetic field with a preexisting field and (2) the untwisting motion was associated with the propagation of torsional Alfvén waves in the corona. In addition, Moore et al. (2015) reported magnetic untwisting in polar coronal hole jets and suggested that the magnetic untwisting wave was a large-amplitude (nonlinear) torsional Alfvén wave. On the basis of the above arguments, we speculate on the possibility of a torsional Alfvén wave in the jet-like structure. If we accept this option, it is possible that the oppositely directed Alfvén waves in the untwisting jet could accelerate the electrons bidirectionally with a 3-minute period.

Alternatively, the torsional waves propagating along the flux rope could change the direction of the field lines to generate a favorable condition for periodic magnetic reconnection between the emerging twisted and preexisting fields (Ning et al. 2004). The generation of torsional waves during reconnection and the associated particle acceleration mechanism in solar flares have been proposed by Fletcher & Hudson (2008).

In conclusion, we reported the possible manifestation of periodic injection of nonthermal electrons bidirectionally in a fan-spine topology during an M-class flare. The acceleration could be periodically modulated by the leakage of sunspot oscillations or by the untwisting motion of a small filament lying under the fan loops. Similar events should be investigated in more detail to reveal the exact trigger mechanism of QPPs in solar flares.

We would like to thank the referee for the positive and constructive comments that improved the manuscript considerably. *SDO* is a mission for the NASA Living With a Star (LWS) program. This work was supported by the “Development of Korea Space Weather Center” of KASI and the KASI basic research funds. The *SDO* data were (partly) provided by the Korean Data Center (KDC) for *SDO* in cooperation with NASA and the *SDO*/HMI team. *RHESSI* is a NASA Small Explorer. The Nobeyama radioheliograph and polarimeters are operated by the National Astronomical Observatory of Japan (NAOJ)/Nobeyama Solar Radio Observatory (NSRO). *Hinode* is a Japanese mission developed and launched by ISAS/JAXA, with NAOJ as domestic partner and NASA and UKSA as international partners. It is operated by these agencies in cooperation with ESA and NSC (Norway). PK thanks Bindu Rani for helpful discussions. K-S Cho acknowledges support by a grant from the US Air Force Research Laboratory, under agreement number FA 2386-14-1-4078 and by the “Planetary system research for space exploration” from KASI. VMN acknowledges the support from the European Research Council under the *SeismoSun* Research Project No. 321141, STFC consolidated grant ST/L000733/1, and the BK21 plus program through the National Research Foundation funded by the Ministry of Education of Korea. The wavelet software was provided by C. Torrence and G. Compo and is available at <http://paos.colorado.edu/research/wavelets/>.

REFERENCES

- Anfinogentov, S., Nakariakov, V. M., Mathioudakis, M., Van Doorsselaere, T., & Kowalski, A. F. 2013, *ApJ*, **773**, 156
 Asai, A., Kiyohara, J., Takasaki, H., et al. 2013, *ApJ*, **763**, 87
 Aschwanden, M. J. 2004, *Physics of the Solar Corona. An Introduction* (Chichester, UK: Praxis Publishing Ltd.)
 Aschwanden, M. J., & Benz, A. O. 1997, *ApJ*, **480**, 825
 Balona, L. A., Broomhall, A.-M., Kosovichev, A., et al. 2015, *MNRAS*, **450**, 956
 Bárta, M., Karlický, M., Vršnak, B., & Goossens, M. 2007, *CEAB*, **31**, 165
 Bárta, M., Vršnak, B., & Karlický, M. 2008, *A&A*, **477**, 649
 Bastian, T. S., Benz, A. O., & Gary, D. E. 1998, *ARA&A*, **36**, 131
 Botha, G. J. J., Arber, T. D., Nakariakov, V. M., & Zhugzhda, Y. D. 2011, *ApJ*, **728**, 84
 Brueckner, G. E., Howard, R. A., Koomen, M. J., et al. 1995, *SoPh*, **162**, 357
 Chen, P. F., & Priest, E. R. 2006, *SoPh*, **238**, 313
 Cheung, M. C. M., De Pontieu, B., Tarbell, T. D., et al. 2015, *ApJ*, **801**, 83
 de Moortel, I. 2009, *SSRv*, **149**, 65
 De Moortel, I., & Nakariakov, V. M. 2012, *RSPTA*, **370**, 3193
 Doyle, J. G., Popescu, M. D., & Taroyan, Y. 2006, *A&A*, **446**, 327
 Fan, Y. 2009, *ApJ*, **697**, 1529

- Fárník, F., Karlický, M., & Švestka, Z. 2003, *SoPh*, **218**, 183
- Fletcher, L., & Hudson, H. S. 2008, *ApJ*, **675**, 1645
- Golub, L., Deluca, E., Austin, G., et al. 2007, *SoPh*, **243**, 63
- Gosling, J. T., Teh, W.-L., & Eriksson, S. 2010, *ApJL*, **719**, L36
- Horne, J. H., & Baliunas, S. L. 1986, *ApJ*, **302**, 757
- Howard, R. A., Moses, J. D., Vourlidas, A., et al. 2008, *SSRv*, **136**, 67
- Hudson, H. S. 2000, *ApJL*, **531**, L75
- Hurford, G. J., Schmahl, E. J., Schwartz, R. A., et al. 2002, *SoPh*, **210**, 61
- Kai, K. 1986, *SoPh*, **104**, 235
- Karlický, M., Bárta, M., & Rybák, J. 2010, *A&A*, **514**, A28
- Kliem, B., Karlický, M., & Benz, A. O. 2000, *A&A*, **360**, 715
- Kumar, P., & Cho, K.-S. 2013, *A&A*, **557**, A115
- Kumar, P., & Cho, K.-S. 2014, *A&A*, **572**, A83
- Kumar, P., Cho, K.-S., Bong, S.-C., Park, S.-H., & Kim, Y. H. 2012, *ApJ*, **746**, 67
- Kumar, P., Innes, D. E., & Inhester, B. 2013, *ApJL*, **779**, L7
- Kumar, P., & Manoharan, P. K. 2013, *A&A*, **553**, A109
- Kumar, P., Nakariakov, V. M., & Cho, K.-S. 2015, *ApJ*, **804**, 4
- Kumar, P., Srivastava, A. K., Somov, B. V., et al. 2010, *ApJ*, **723**, 1651
- Kundu, M. R. 1961, *JGR*, **66**, 4308
- Kundu, M. R. 1965, *Solar Radio Astronomy* (New York: Interscience Publications)
- Kundu, M. R., White, S. M., Gopalswamy, N., & Lim, J. 1994, *ApJS*, **90**, 599
- Lee, E. J., Archontis, V., & Hood, A. W. 2015, *ApJL*, **798**, L10
- Lemen, J. R., Title, A. M., Akin, D. J., et al. 2012, *SoPh*, **275**, 17
- Lin, R. P., Dennis, B. R., Hurford, G. J., et al. 2002, *SoPh*, **210**, 3
- Liu, W., & Ofman, L. 2014, *SoPh*, **289**, 3233
- Liu, W., Ofman, L., Nitta, N. V., et al. 2012, *ApJ*, **753**, 52
- Longcope, D. W., & Welsch, B. T. 2000, *ApJ*, **545**, 1089
- Masson, S., Pariat, E., Aulanier, G., & Schrijver, C. J. 2009, *ApJ*, **700**, 559
- Mathioudakis, M., Seiradakis, J. H., Williams, D. R., et al. 2003, *A&A*, **403**, 1101
- Metcalfe, T. R., Hudson, H. S., Kosugi, T., Puetter, R. C., & Pina, R. K. 1996, *ApJ*, **466**, 585
- Moore, R. L., Sterling, A. C., & Falconer, D. A. 2015, *ApJ*, **806**, 11
- Nakajima, H., Nishio, M., Enome, S., et al. 1994, *IEEEP*, **82**, 705
- Nakajima, H., Sekiguchi, H., Sawa, M., Kai, K., & Kawashima, S. 1985, *PASJ*, **37**, 163
- Nakariakov, V. M., Foullon, C., Verwichte, E., & Young, N. P. 2006, *A&A*, **452**, 343
- Nakariakov, V. M., Inglis, A. R., Zimovets, I. V., et al. 2010, *PPCF*, **52**, 124009
- Nakariakov, V. M., & Melnikov, V. F. 2009, *SSRv*, **149**, 119
- Nakariakov, V. M., & Zimovets, I. V. 2011, *ApJL*, **730**, L27
- Ning, Z., Innes, D. E., & Solanki, S. K. 2004, *A&A*, **419**, 1141
- Pandey, J. C., & Srivastava, A. K. 2009, *ApJL*, **697**, L153
- Pariat, E., Antiochos, S. K., & DeVore, C. R. 2010, *ApJ*, **714**, 1762
- Pascoe, D. J., Nakariakov, V. M., & Kupriyanova, E. G. 2013, *A&A*, **560**, A97
- Pesnell, W. D., Thompson, B. J., & Chamberlin, P. C. 2012, *SoPh*, **275**, 3
- Pontin, D. I., Priest, E. R., & Galsgaard, K. 2013, *ApJ*, **774**, 154
- Pugh, C. E., Nakariakov, V. M., & Broomhall, A.-M. 2015, *ApJL*, **813**, L5
- Roberts, B. 2000, *SoPh*, **193**, 139
- Scargle, J. D. 1982, *ApJ*, **263**, 835
- Schou, J., Scherrer, P. H., Bush, R. I., et al. 2012, *SoPh*, **275**, 229
- Sych, R., Nakariakov, V. M., Karlický, M., & Anfinogentov, S. 2009, *A&A*, **505**, 791
- Tajima, T., Sakai, J., Nakajima, H., et al. 1987, *ApJ*, **321**, 1031
- Takasao, S., Asai, A., Isobe, H., & Shibata, K. 2012, *ApJL*, **745**, L6
- Takasao, S., Matsumoto, T., Nakamura, N., & Shibata, K. 2015, *ApJ*, **805**, 135
- Torrence, C., & Compo, G. P. 1998, *BAMS*, **79**, 61
- Tsuneta, S., Ichimoto, K., Katsukawa, Y., et al. 2008, *SoPh*, **249**, 167
- Wang, H., & Liu, C. 2012, *ApJ*, **760**, 101
- White, S. M., Krucker, S., Shibasaki, K., et al. 2003, *ApJL*, **595**, L111
- Wuelser, J.-P., Lemen, J. R., Tarbell, T. D., et al. 2004, *Proc. SPIE*, **5171**, 111
- Yashiro, S., Gopalswamy, N., Michalek, G., St., et al. 2004, *JGRA*, **109**, 7105